A 0-D model for orificed hollow cathodes with application to the scaling of total pressure

Pierre-Yves C. R. Taunay,* Christopher J. Wordingham,*

Edgar Y. Choueiri†

Princeton University, Princeton, NJ, 08544, USA

A scaling relationship for the total pressure inside orificed hollow cathodes is derived from a theoretical zero-dimensional model from which plasma quantities are computed, including the total pressure. The variation of total pressure with controllable parameters must be properly evaluated because it is critical for determining the lifetime of thermionic inserts. The model is based on the conservation of energy and momentum for the combined plasma-neutral fluid and on the assumption of charge-exchange-dominated ambipolar diffusion in the insert region plasma. The controllable inputs of the model are the cathode geometry, the gas species used, and the operating conditions (discharge current and mass flow rate). The neutral gas temperature and sheath potential are two non-controllable parameters. Good agreement is obtained with pressure data from the literature and new experimental total pressure data measured at up to 300 A of discharge current in a large hollow cathode. A scaling relationship for the total pressure is derived from the plasma fluid momentum balance and the numerical results of the theoretical model. The total pressure is found to scale with the square of the mass flow rate multiplied by a weak function of discharge current, and with the square of the discharge current. The nature of the scaling is interpreted physically to be due to the relative importance of the magnetic pressure and the gasdynamic pressure modified to take into account the plasma contribution to the orifice speed of sound.

List of Symbols

Constants

μ_0	Permeability of vacuum	$4\pi \times 10^{-7}$ H/m
C	Electron-ion collision frequency constant 2.9×10^{-12}	
e	Elementary charge	1.602×10^{-19} C
k_B	Boltzmann's constant	1.38×10^{-23} J/K
m	Electron mass	9.1×10^{-31} kg

Circuit parameters

I_d	Discharge current	A
R_p	Plasma resistance	Ω

Geometry

L_{emit}	Emission length	m
L_o	Orifice length	m
r_c	Cathode (insert) radius	m
r_o	Orifice radius	m

Plasma parameters

α	Ionization fraction	
$\ln \Lambda$	Coulomb Logarithm	
ϕ_s	Sheath potential	V
f_s	Ratio of sheath-edge to volume-average electron density	
I_i	Ion current	A
I_r	Random electron current	A

---

*Graduate Student, MAE Dept., Princeton University, AIAA Student Member — ptaunay@princeton.edu
†Chief Scientist, EPPDyL, Professor, Applied Physics Group, MAE Dept., Princeton University, AIAA Fellow.

American Institute of Aeronautics and Astronautics

Symbol	Description	Unit	Symbol	Description	Unit
I_{em}	Thermionic current	A	ϵ_i	Ionization energy	eV
n_e	Electron density	m^{-3}	ϵ_{ex}	Excitation energy	eV
n_e^s	Sheath-edge electron density	m^{-3}	M	Ion or neutral particle mass	kg
n_g	Neutral gas density	m^{-3}	**Flow properties**		
T_e	Electron temperature	K	$\dot{m}$	Mass flow rate	kg/s
T_g	Neutral gas temperature	K	γ	Ratio of heat capacities	
T_{eV}	Electron temperature	V	$\mathbf{v_g}$	Neutral fluid velocity	m/s
v_B	Bohm velocity	m/s	$\mathbf{v_i}$	Ion fluid velocity	m/s
Collisions			$\mathbf{v}$	Mean mass fluid velocity	m/s
ν_{ei}	Electron-ion collision frequency	s	ρ	Mean mass density	kg/m^3
ν_{en}	Electron-neutral collision frequency	s	Kn	Knudsen number	
σ_{en}	Electron-neutral collision cross section	m^2	Re	Reynolds number	
σ_{ex}	Excitation cross section	m^2	a	Speed of sound	m/s
σ_{iz}	Ionization cross section	m^2	P	Total pressure	Pa
Thermionic emission			P_{exit}	Orifice outlet exit pressure	Pa
ϕ_w	Surface work function	V	P_{gd}	Gasdynamic pressure	Pa
D_{RD}	Richardson-Dushman constant	A/(m$^2{\cdot}$K^2)	P_{mag}	Magnetic pressure	Pa
T_c	Cathode wall temperature	K	P_{mf}	Orifice plate momentum flux	Pa
Gas properties			R_g	Gas constant	J/(kg$\cdot$K)

I.   Introduction

Reliable operation of hollow cathode electron sources is critical for successful long-term operation of Hall and ion thrusters. Both lifetime and operational power requirements for these thrusters continue to increase. "Near-term" next-generation thrusters are expected to operate at discharge powers of $100-200$ kW[1] with proposed missions that require operational lifetimes of up to 100 kh.[2,3] Cathode discharge currents approaching 700 A may be required[4,5] for specific impulses in the range of 2000 to 6000 s. Existing thrusters are starting to approach or exceed this power level.[6,7] Discharge currents of up to 400 A have been demonstrated,[8,9] with expected cathode lifetime in the range of 10 to 20 kh.[9] However, without experimental measurements of the emitter temperature profile and internal axial plasma density profile, it is challenging to predict the operational lifetime. Robust cathode models that are widely-applicable and that do not use cathode-specific experimental data for input are necessary for the development of next-generation hollow cathodes.

The neutral gas pressure in an orificed hollow cathode affects physical quantities such as the ratio of sheath-edge plasma density to average plasma density and electron temperature,[10,11] and, therefore, the total lifetime of the insert. The electron temperature depends only on the geometry of the cathode and the neutral gas density (or pressure for a constant temperature) if ambipolar diffusion is assumed to be charge-exchange-dominated.[11] It is critical to obtain an accurate value of the neutral gas pressure to ensure that the lifetime of the thermionic insert is maximized. To estimate the neutral gas pressure, both the total pressure and ionization fraction can be used. Multiple models exist to estimate the total pressure: empirical relationships, designed for a mercury hollow cathode[12–17] or based on the available data from the literature,[18] isentropic[19] or isothermal[20,21] flow approaches, Poiseuille flow theory,[22–24] a modification of Poiseuille flow theory,[25,26] and an "equivalent temperature" or modified specific gas constant taking into

account the ionization fraction.[20, 21, 27, 28] The ionization fraction may be estimated through a zero-dimension model.

We have shown in Ref. 18 that the empirical relationship developed by Siegfried *et al.* does not generalize to other cathodes and that the assumptions of isentropic, isothermal, or viscous Poiseuille flow are invalid in the flow regime in which cathodes operate. The empirical relationship we proposed in Ref. 18 covers available data from the literature but may not generalize to new designs unless they are similar to cathodes included in the analysis used to derive the relationship. It is also limited by its data-driven approach which does not explain the physical phenomena governing the total pressure in orificed hollow cathodes. In our extensive review of 0-D cathode models[10] we have also shown that current models cannot be applied to cathodes that are different from the design for which they were originally developed. It is therefore not possible to use those models to estimate the ionization fraction for a wide variety of cathodes and operating conditions.

In this work, we propose a theoretical zero-dimension model to calculate all plasma quantities in a cathode that addresses the critical issues of 0-D models found in Ref. 10. The model is based on conservation of energy for the electron fluid, conservation of momentum for the plasma fluid (both neutral and charged particles), and electron temperature and attachment length results from Ref. 11. We first present our experimental setup and discuss the assumptions of the theoretical model. We then delineate the theoretical model and show that our results agree with experimental data on a variety of cathodes. We finally use the model to derive a scaling relationship for the total pressure and we interpret the physical nature of this scaling.

II.   Experimental setup

A.   Cathode configuration

The Princeton large hollow cathode (PLHC) is a 20 cm long (8-in.) cathode with an inner bore of 3.26 cm (1.284-in.). The cathode material is AXM-5Q POCO graphite. The PLHC features a 2.715 cm inner diameter, 8.04 cm long lanthanum hexaboride (LaB$_6$) insert. The insert is heated via an external graphite heater described in Ref. 29. A heat shield made of multiple layers of 200 μm (0.008-in.) thick grafoil and of 50 μm (0.002-in.) thick molybdenum is used to reduce radiative heat loss. The cathode has a tungsten orifice plate which is 1.5 mm thick and which has a 5.6 mm (7/32-in.) diameter orifice. The cathode is mounted on a block of 253MA stainless steel and is held in place by a clamp ring of the same material. Interfaces between materials are sealed with graphite gaskets.

In front of the cathode is a 6.35 mm (1/4-in.) thick graphite keeper plate with a 9.52 mm (3/8-in.) diameter orifice and a water-cooled, aluminum anode. Figure 1a shows the cathode, anode, and heater. The cathode with keeper and heat shielding installed is shown in Fig. 1b.
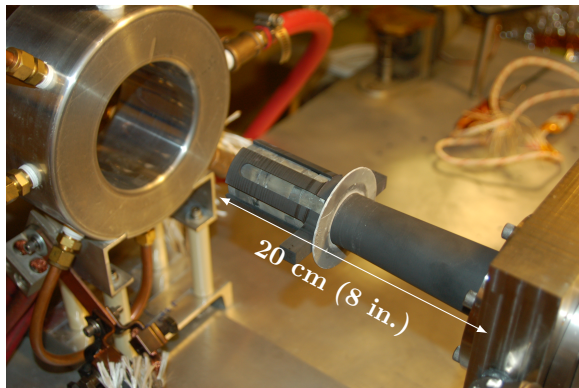
(a) Cathode without heat shield.

(b) Cathode with heat shield.

Figure 1: Princeton large hollow cathode.

B.   Facilities

The cathode is installed in a 2 m diameter by 5 m long vacuum vessel evacuated to less than 7×10^{-5} Torr without gas flow, or 2×10^{-4} Torr at the maximum tested flow rate (290 sccm of argon). The graphite heater is powered by a 13.3 kW American Reliance power supply with a maximum output of 32 V or 400 A. In all of our experiments the cathode operates in triode mode (cathode, keeper, anode). The cathode discharge is sustained by a 30 kW Miller SRS-1000-C1 welding power supply configured for a maximum output of 150 V or 500 A. A 50 Ω resistor is used upstream of the keeper to limit the total keeper current to 3 A. The total current from the power supply is controlled with a manual dial. An electrical diagram of the setup is shown in Fig. 2. The experimental circuit features current shunts R_c, R_a, R_k, and R_h that are used to measure the current flowing through the cathode, anode, keeper, and heater, respectively.
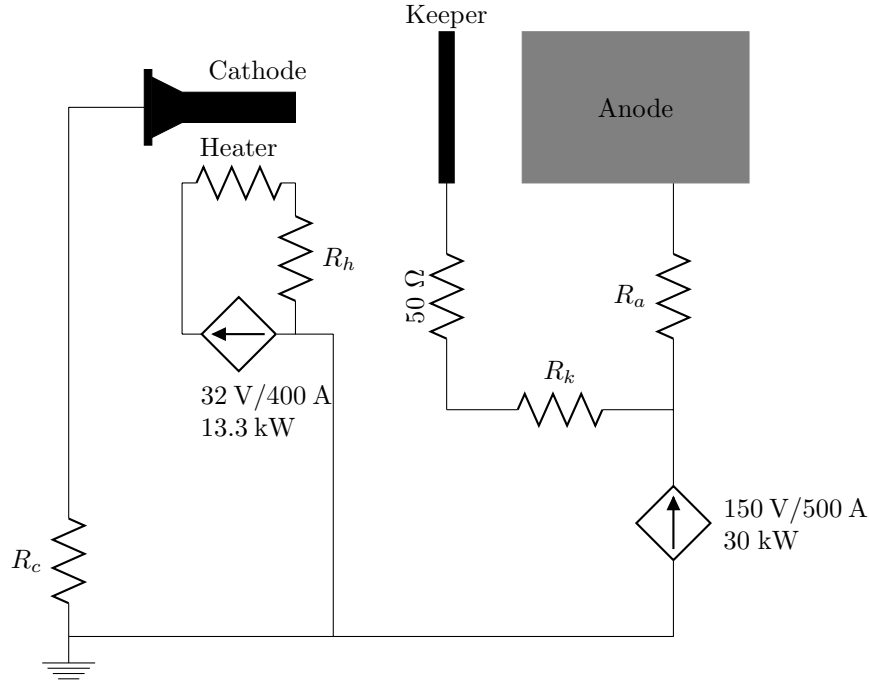

Figure 2: Electrical diagram of the experiment.

C.   Measurement system

We measure the total pressure upstream of the cathode with a Posifa PVC1000 Pirani gauge connected to the stainless steel support block through a 3/8-in. NPT fitting. The pressure tap is located approximately 22 cm (8.75 in.) from the upstream surface of the cathode orifice. The housing of the Pirani gauge is water-cooled to keep the gauge below its maximum operating temperature. The Pirani gauge is powered by a custom-built ultra-precision constant-current power supply (6.7 mA). We calculate the pressure using the measured resistance of the MEMS gauge resistor. The gauge was calibrated to within ± 0.1 Torr for argon gas with a separate MKS baratron gauge.

A National Instruments (NI) NI-9206 data acquisition system (DAQ) is used to perform differential voltage measurement across the Pirani gauge and current shunts. The NI-9206 is attached to a NI-cDAQ 9274 chassis which is used to communicate via USB to a computer. The voltage difference across each current shunt is amplified by an AD623 instrumentation amplifier before being measured by the DAQ. Special care is taken for the high-side current shunts (keeper and anode); because the operating voltages of both the anode and keeper are higher than that tolerated by our DAQ, we isolate these measurements with an HCPL-7520 isolation amplifier.

American Institute of Aeronautics and Astronautics

III. Theory

In this section we present a theoretical framework to explain the variation of total pressure with mass flow rate, discharge current, cathode geometry, and gas species. The main assumptions for our analysis are given in the following section. We then delineate the fluid and plasma models.

A. Assumptions

We make the following assumptions:

1. The plasma is treated as a continuum fluid in the insert and orifice regions.

2. The heavy-particle stagnation temperature in both regions is constant and is a free parameter.

3. The flow in the orifice is frozen.

4. The total static pressure is constant in the insert region.

5. The flux of ions to the walls is equal to the Bohm flux and is not modified by the presence of an emitting sheath.

6. The fluid is inviscid.

7. The electron temperature is constant in each region.

8. The electron inertia is negligible compared to that of the heavy species.

9. Inelastic collisions other than direct ionization and ground-state excitation are ignored.

10. Steady-state conditions are reached.

Our first assumption is justified for cathodes with a small orifice-to-insert diameter ratio (*i.e.*, most orificed hollow cathodes).[18] The Knudsen number is generally less than 1 for those cathodes. This assumption is invalid when the flow becomes molecular, such as in the downstream portion of the orifice, in cathodes that have an orifice-to-insert diameter ratio close to 1 (*i.e.*, tube cathodes), and in cathodes with a low mass flow rate. We use empirical corrections to compensate for transitional flow effects at the orifice outlet. The second assumption implies that the ion and neutral static temperatures are equal, which is justified because of the large cross section for resonant charge exchange between heavy species in noble gases. We specify the static temperature in the orifice region and calculate the stagnation temperature under the assumption of an adiabatic flow. It is challenging to experimentally obtain the temperature of the neutral particles or ions in either the insert or orifice regions, and it is therefore difficult to evaluate the validity of the second assumption. This assumption is nonetheless used in most cathode models.[19, 22–24, 30–35]

Because the mean free path for inelastic electron-neutral collisions is much larger than the orifice size, and because the residency time is smaller than the time between inelastic collisions for neutral particles in the orifice, the assumption of frozen flow (assumption 3) is justified. The ratio of mean free path to orifice length L_o and the ratio of inter-collision time to residency time for the neutrals are given by

$$\bar{\lambda} = \frac{1}{n_e \sigma \left(T_{eV}\right) L_o},$$ (1)

and

$$\bar{\tau} = \frac{v_g}{L_o} \frac{1}{n_e \left\langle \sigma \left(T_{eV}\right) v \right\rangle} = \frac{v_g}{v_e} \bar{\lambda},$$ (2)

respectively. n_e is the electron density, σ is the inelastic reaction cross section, T_{eV} is the electron temperature, v_g is the local sound speed, and v_e is the average electron velocity. Figure 3 shows the two ratios for xenon and two orifice aspect ratios Λ_{or} (orifice length over orifice diameter), where we assume a gas temperature of 2,000 K to calculate the speed of sound. The electron temperature is calculated from the neutral gas density using the ambipolar diffusion model from Ref. 11. The excitation cross section is computed from the sum of all excited states. The mean free path for inelastic collisions is much longer than the orifice length for all neutral densities of interest. As indicated by the variation of the ratio of inter-collision time to neutral gas residency time, the frozen flow approximation may be challenged for large orifice aspect ratios.
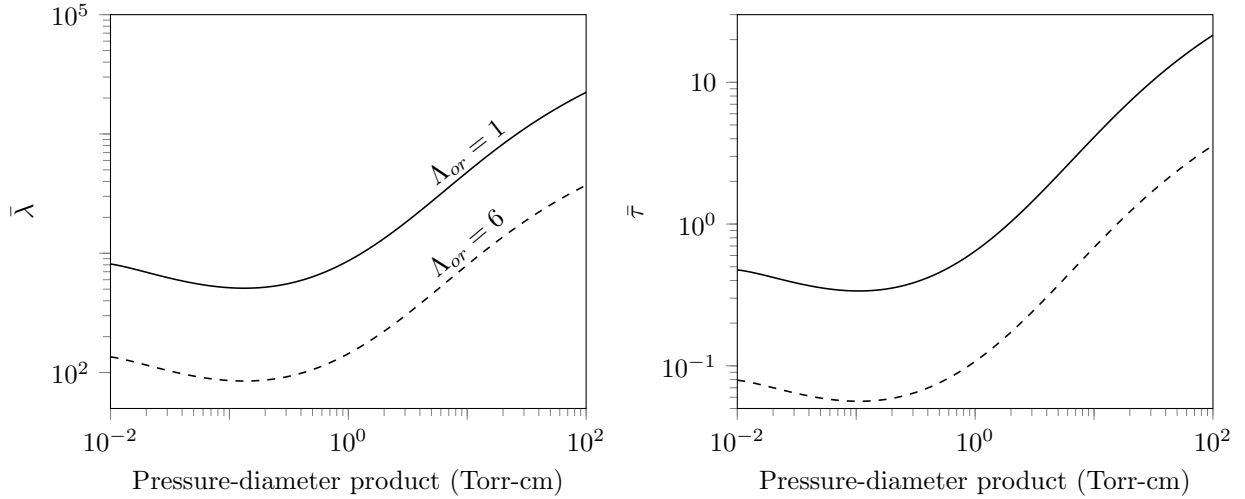
American Institute of Aeronautics and Astronautics

Figure 3: Left: Ratio of mean free path to orifice length for total inelastic electron-neutral collisions. Right: ratio of inter-collision time to neutral gas residency time.

The likelihood that a neutral atom undergoes many inelastic collisions before exiting the orifice channel is then very high. In general, however, this approximation allows us to provide a bound on the flow variables.

Assuming a constant total static pressure (assumption 4) in the insert region is justified because pressure gradients are small in the insert region for cathodes with small orifice-to-insert-diameter ratio. We note, however, that pressure gradients occur near the orifice inlet, where the flow is constricted. The flow gains kinetic energy at the expense of pressure energy in this region. The pressure difference between the upstream section and the orifice plate results in an additional force which increases the momentum flux through the orifice.[36] Ignoring this effect should result in an under-prediction of the total pressure.

It is necessary to estimate the flux of ions to the walls to include particle effects in the fluid model. Assuming that ions achieve the Bohm velocity at the edge of an emitting sheath (assumption 5) is not necessarily justified[10] but it is a common assumption to all cathode models. Using the model from Ref. 37 it is possible to estimate the modification of the Bohm velocity by an emitting sheath. For typical cathode current densities, the presence of an emitting sheath may modify the Bohm velocity by up to 20%.

Neglecting the viscosity (assumption 6) is motivated by the statistical analysis presented in Ref. 18. This study showed that viscous effects on the total pressure are likely negligible as compared to gasdynamic and plasma effects. Viscosity can nonetheless be implemented by considering that most of the viscous losses come from the feed system. Experimental measurements of the pressure data we used are gathered upstream of the insert region (sometimes multiple cathode lengths away, see, *e.g.*, Ref. 25). This means that the viscous pressure drop within the feed system contributes to the measured total pressure. A Poiseuille flow assumption is justified in this section: the flow is neutral, isothermal, viscous, laminar, incompressible, fully-developed, and not near a constriction. We use the heavy-particle temperature as the effective gas temperature when estimating the viscous losses in the feed system.

Experimental data[13, 21, 38–40] suggest that the assumption of constant electron temperature (assumption 7) in the insert region is appropriate. We do not expect large gradients in electron temperature the orifice region. In effect, this assumption means that the fluid is isothermal in each individual region.

B. Fluid model

We use the two-dimensional axisymmetric momentum equations for each species, applied to the geometry shown in Fig. 4. Boundaries II, III, and IV are chosen to be at the sheath edge. The emission length, L_{emit}, is the length over which the plasma is able to support temperature-limited thermionic emission. We approximate this length with the plasma density decay length scale in the axial direction, as calculated in Ref. 11. The emission length is smaller the insert length and we consider that the fluid is neutral upstream of the emission zone.

The momentum equations for each species are summed to provide a simpler single-fluid framework. Under

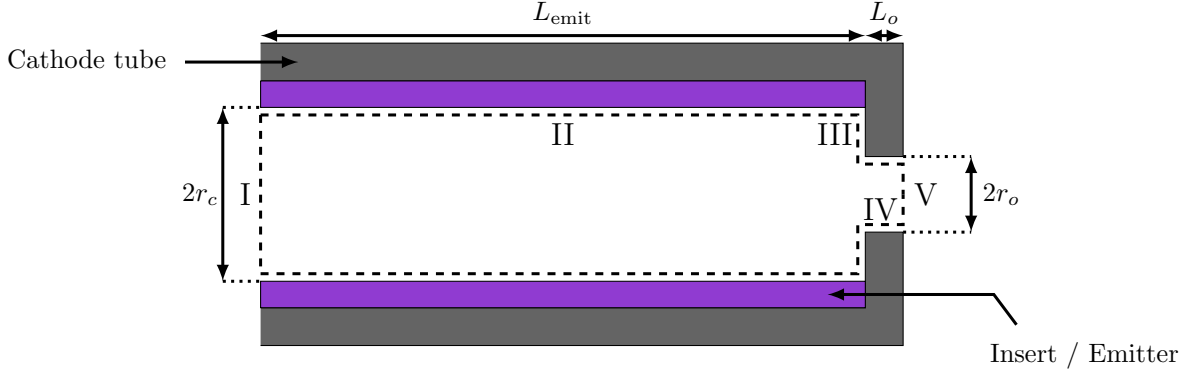American Institute of Aeronautics and Astronautics

Figure 4: Fluid control volume considered in the analysis.

the assumptions delineated in the previous section, we obtain:

$$\nabla \cdot (\rho \mathbf{v}\mathbf{v}) + \nabla P = \nabla \cdot \underline{\underline{\boldsymbol{\beta}}}, \tag{3}$$

where $\mathbf{v}$ is the mean mass velocity of the combined fluid, ρ its density, and $\underline{\underline{\boldsymbol{\beta}}}$ the magnetic stress tensor. P is the total static pressure. Equation 3 may also be written as

$$\nabla \cdot (M n_g \mathbf{v_g}\mathbf{v_g} + M n_e \mathbf{v_i}\mathbf{v_i}) + \nabla P = \nabla \cdot \underline{\underline{\boldsymbol{\beta}}}, \tag{4}$$

where the subscripts g, e, and i denote neutral, electron, and ion quantities, respectively. n_x and $\mathbf{v_x}$ are the number density and velocity of the species x, respectively. M is the mass of the heavy particles.

To satisfy conservation of mass, ions return to the control volume as neutrals after having recombined on any of the sheath-facing surfaces (II, III, and IV). The flux of each species is therefore equal in magnitude and opposite in direction:

$$n_g v_g = -n_e^s v_B, \tag{5}$$

where n_e^s is the electron density at the sheath edge.

An upper-bound on the magnetic pressure on surfaces III and V can be obtained by considering that the magnetic field $\underline{\mathbf{B}}$ on these surfaces is due only to the current flowing through the orifice, which is assumed to be purely axial. The magnetic field is then purely azimuthal:

$$\underline{\mathbf{B}} = (0, B_\theta, 0)_{(\hat{r}, \hat{\theta}, \hat{z})} . \tag{6}$$

The magnetic stress tensor can then be expressed as:[41]

$$\underline{\underline{\boldsymbol{\beta}}} = \begin{bmatrix} -B_\theta^2/2\mu_0 & 0 & 0 \\ 0 & B_\theta^2/2\mu_0 r^2 & 0 \\ 0 & 0 & -B_\theta^2/2\mu_0 \end{bmatrix}, \tag{7}$$

where μ_0 is the permeability of vacuum. The azimuthal component of the magnetic field can be estimated by further assuming constant current density in the orifice:

$$B_\theta = \begin{cases} -\dfrac{\mu_0 I_d}{2\pi r} & \text{if } r > r_o \\[2mm] -\dfrac{\mu_0 I_d}{2\pi r_o^2} r & \text{if } r < r_o \end{cases} \tag{8}$$

where r_o is the orifice radius and I_d is the discharge current.

We integrate Equation 4 over the volume shown in Fig. 4, and apply Gauss's theorem. In the z-direction, we obtain:

$$-\left[\pi r_c^2 P\right]_{\mathrm{I}} + \pi \left(r_c^2 - r_o^2\right) \left[P + M n_e^s v_B^2 \left(\frac{n_e^s}{n_g} + 1\right)\right]_{\mathrm{III}} + \pi r_o^2 \left[\rho v_z^2 + P\right]_{\mathrm{V}} = -\frac{\mu_0 I_d^2}{4\pi}\left(\ln\frac{r_c}{r_o} + \frac{1}{4}\right), \tag{9}$$

where r_c is the insert radius and v_z is the fluid velocity on the surface V. To obtain Eqn. 9 we further assumed that

- the upstream momentum is negligible as compared to the static pressure contribution,

- surface quantities other than the magnetic field are constant over their respective surfaces,

- the heavy particles have equal tangential velocity on each surface, and

- the radial velocity of the heavy particles on surface V is much smaller than the axial one.

The third assumption combined with the flux condition given in Eqn. 5 causes the cross-term in the dyad product to vanish. For example, on surface II, the cross-term resulting from the momentum balance in the axial direction is

$$D = M n_e^s v_{i,r} v_{i,z} + M n_g v_{g,r} v_{g,z}.$$

Because the particle fluxes normal to the wall are equal in magnitude and in opposite direction (Eqn. 5), we have

$$D = M n_e^s v_B \left(v_{i,z} - v_{g,z} \right).$$

The assumption of equal tangential velocity, motivated by frequent collisions between ions and neutrals, implies that $v_{i,z} = v_{g,z}$ on this surface. The dyad terms then simplify to zero. $\square$

OUTLET (V) The frozen-flow approximation allows us to define the Mach number and specific heat ratio γ. Under this assumption, the flow is choked and becomes sonic at the exit of the orifice because it expands into a vacuum. The flow velocity is therefore given by the local speed of sound a for the combined fluid:

$$v_{z,\mathrm{V}} = a = \sqrt{\gamma R_g \left(T_g + \alpha T_e \right)}, \tag{10}$$

where R_g is the gas constant of neutral species, α is the ionization fraction, and T_g and T_e are the neutral and electron temperatures in Kelvin, respectively. This expression can be readily derived for an ideal gas where $a = \sqrt{\gamma P / \rho}$. The ionization fraction is defined as:

$$\alpha = \frac{n_e}{n_e + n_g}. \tag{11}$$

Using the conservation of mass, we also have $\pi r_o^2 \left(\rho v_z \right)_{\mathrm{V}} = \dot{m}$.

Because the Knudsen number in the orifice, Kn, is within the range of $0.1 - 10$ the flow is considered transitional. We therefore estimate P_{V} with a molecular flow correction. We use a similar framework to Refs. 42–44. Under the assumption that the pressure downstream of the cathode orifice (vacuum vessel pressure) is much smaller than the exit plane pressure, the stagnation pressure P_{V}^* is given by

$$P_{\mathrm{V}}^* = \frac{\dot{Q}}{\left(\theta C_m + \left(1 - \theta \right) C_v \right)}, \tag{12}$$

where $\dot{Q}$ is the total throughput and C_m and C_v are the molecular flow and viscous flow aperture conductances, respectively. The linear weight θ is a function of the Knudsen number. The expression proposed in Ref. 42 can be written as suggested by Refs. 43 and 44:

$$\theta = \frac{k_\theta \mathrm{Kn}}{k_\theta \mathrm{Kn} + 1}, \tag{13}$$

where $k_\theta = 28$. This value of k_θ corresponds to equal weighing of molecular and viscous flows ($\theta \approx 0.5$) when the average pressure in the orifice is equal to the midpoint pressure of the transition range.[42] This corresponds to $\mathrm{Kn} \approx 0.04$. The throughput and the conductance of the orifice aperture for the flow is given by

$$\dot{Q} = \frac{k_B}{M} T_g \left(\frac{\gamma + 1}{2} \right) \dot{m}, \text{ and} \tag{14}$$

$$C_a = \pi r_o^2 \sqrt{\left(\frac{\gamma + 1}{2} \right) \frac{k_B T_g}{2\pi M}}, \tag{15}$$

respectively. The $(\gamma + 1)/2$ term comes from the conversion from static to stagnation quantities in the insert region. Because the throughput is referenced to upstream stagnation quantities, the plasma contribution to the sound speed does not appear in $\dot{Q}$. The molecular and viscous flow conductances are[42, 43]

$$C_m = C_a \left(\frac{2}{\gamma + 1}\right)^{1/2}, \text{ and} \tag{16}$$

$$C_v = \sqrt{2\pi} \left(\gamma \left(\frac{2}{\gamma + 1}\right)^{(\gamma+1)/(\gamma-1)}\right)^{1/2} C_a, \tag{17}$$

respectively. The static pressure on surface V is retrieved from the definition of the stagnation pressure at a Mach number of 1:

$$P_{\mathrm{V}} = P_{\mathrm{V}}^* \left(\frac{2}{\gamma + 1}\right)^{\gamma/\gamma-1}. \tag{18}$$

ORIFICE PLATE (III)   Because we have assumed a constant total pressure in the insert volume, the total static pressure on the orifice plate is equal to that at the inlet: $P_{\mathrm{III}} = P_{\mathrm{I}}$.

COMBINED EXPRESSION   We reorganize Equation 9 to obtain an expression for the total (static) pressure:

$$P = P_{mag} + P_{gd} + P_{mf} + P_{\mathrm{exit}} \tag{19}$$

where P_{mag}, P_{gd}, P_{mf}, P_{exit} are the magnetic pressure on surfaces III and V, gasdynamic pressure contribution, orifice plate momentum flux, and orifice outlet exit pressure, respectively. These quantities are defined as

$$P_{mag} = \frac{\mu_0 I_d^2}{4\pi^2 r_o^2} \left(\ln \frac{r_c}{r_o} + \frac{1}{4}\right), \tag{20}$$

$$P_{gd} = \frac{\dot{m}}{\pi r_o^2} \sqrt{\gamma R_g \left(T_g + \alpha_o T_e\right)}, \tag{21}$$

$$P_{mf} = \left(\frac{r_c^2}{r_o^2} - 1\right) e n_e^s T_{eV} \left(1 + \frac{n_e^s}{n_g}\right), \text{ and} \tag{22}$$

$$P_{\mathrm{exit}} = P_{\mathrm{V}}^* \left(\frac{2}{\gamma + 1}\right)^{\gamma/\gamma+1}, \tag{23}$$

respectively. For P_{mf}, n_e^s and T_{eV} are calculated using insert-region quantities. The fluid speed of sound appearing in the gasdynamic pressure is computed with orifice-region quantities. α_o denotes the ionization fraction in the orifice.

Equation 19 states that the total static pressure upstream of the cathode emission zone is the balance between the particle momentum leaving the volume, the magnetic pressure, and the downstream static pressure.

C.   Plasma model

To close the system of equations, estimates of the degree of ionization, neutral density, and electron temperature are required for both the insert and orifice regions. In the insert region an estimate of the attachment length, or length over which the plasma is dense enough to support temperature-limited thermionic emission, is also required. Because the ionization fraction may not be negligible (especially in the orifice region) we do not employ the typical approximation $\alpha \ll 1$; we retain all terms in the resulting equations in both regions. For all of our calculations, the collision frequencies are computed using Maxwellian-averaged collision cross sections.

1.   Electron temperature and attachment length

We employ the method delineated in Ref. 11 to calculate the electron temperature in both insert and orifice regions, as well as the attachment length. The method is based on a charge-exchange-limited ambipolar diffusion model of the plasma. Application of this method gives an analytical approximation of the attachment

American Institute of Aeronautics and Astronautics

length and the electron temperature in both regions as functions of the neutral-pressure-diameter product only. We define the "attachment length" as the plasma density decay length-scale for the first-order eigenmode of the full 2D solution in the insert. The insert electron temperature is not sensitive to the neutral gas temperature in that region; we therefore ran the 2D solution with an assumed neutral gas temperature of 3,000 K in the insert region. The orifice electron temperature, however, can vary by up to 20% with a change in neutral gas temperature. The solution is therefore calculated with multiple neutral gas temperatures.

We use the following approximations for the insert and orifice electron temperature,

$$T_{eV}^{\text{insert}} = \frac{t_{i,0}}{(n_g k_B T_g (2r_c))^{t_{i,1}}} + t_{i,2}, \tag{24}$$

$$T_{eV}^{\text{orifice}} = \frac{t_{o,0}}{(n_g k_B T_g (2r_c))^{t_{o,1}} + t_{o,2}} + t_{o,3}, \tag{25}$$

and for the attachment length,

$$L_{\text{emit}} = r_c \left(l_0 + \frac{l_1}{\ln^6 (n_g k_B T_g (2r_c) + l_2)} \right), \tag{26}$$

respectively. The coefficients $t_{i,k}$, $t_{o,k}$, and l_k for xenon and argon gases are shown in the Appendix. In all cases, the pressure-diameter product that appears in the denominator is in Torr-cm.

2. Insert region

The conservation of charge in the insert region gives the total discharge current I_d as

$$I_d = I_i + I_{em} - I_r, \tag{27}$$

where I_i, I_{em}, and I_r are the ion, thermionic, and random electron currents, respectively. Assuming that all ions created in the volume go to the insert wall, the ion current is either given by its volumetric definition, or by its value at the sheath edge,

$$I_i = e n_g n_e < \sigma_{iz} v > \pi L_{\text{emit}} r_c^2 = e n_e^s v_B 2\pi r_c L_{\text{emit}}, \tag{28}$$

where σ_{iz} is the ionization cross-section. Using Eqn. 28, we obtain the sheath-edge density:

$$n_e^s = \frac{n_g n_e < \sigma_{iz} v > r_c}{2 v_B} = \frac{\alpha}{1 - \alpha} \frac{n_g^2 < \sigma_{iz} v > r_c}{2 v_B}. \tag{29}$$

We use this result to define f_s, the ratio between the sheath-edge and the volume-averaged electron density, as a function of volume-averaged quantities:

$$f_s = \frac{n_g < \sigma_{iz} v > r_c}{2 v_B}. \tag{30}$$

The random electron current can be expressed in terms of volumetric quantities:

$$I_r = e \frac{1}{4} \left(\frac{8M}{\pi m} \right)^{1/2} n_g n_e < \sigma_{iz} v > \pi L_{\text{emit}} r_c^2 \exp \left(-\phi_s / T_{eV} \right), \tag{31}$$

where m is the mass of the electron and ϕ_s is the sheath potential.

We integrate the electron energy equation over a cylindrical volume of length L_{emit} and radius r_c with the face fluxes estimated using a zeroth-order upwind scheme as suggested in Ref. 22. We obtain

$$I_{em} \phi_s + R_p I_d^2 = I_i \epsilon_i + \frac{5}{2} T_{eV} I_d + (2 T_{eV} + \phi_s) I_r, \tag{32}$$

where ϵ_i is the ionization energy of the species of interest, and R_p is the plasma resistance. The plasma resistance is given by

$$R_p = \frac{m}{n_e e^2} \frac{L_{\text{emit}}}{\pi r_c^2} (\nu_{ei} + \nu_{en}), \tag{33}$$

where ν_{ei} and ν_{en} are the electron-ion and electron-neutral collision frequencies, respectively.

We use the conservation of charge (Eqn. 27) to eliminate the thermionic current terms from the electron energy equation. The resulting equation is expressed in terms of the ionization fraction and the neutral gas density by replacing the electron density with the definition of the ionization fraction (Eqn. 11). This yields a quadratic expression for the unknown ionization fraction:

$$\alpha^2 \left[e n_g^2 < \sigma_{iz} v > \pi L_{\text{emit}} r_c^2 \left(\epsilon_i + \phi_s + 2 T_{eV} \frac{1}{4} \left(\frac{8M}{\pi m} \right)^{1/2} \exp\left(-\phi_s/T_{eV}\right) \right) + e n_g^2 < \sigma_{ex} v > \pi L_{\text{emit}} r_c^2 \epsilon_{ex} \right.$$

$$\left. + \frac{m L_{\text{emit}}}{\pi r_c^2 e^2} C \ln \Lambda T_{eV}^{-3/2} I_d^2 - I_d \left(\frac{5}{2} T_{eV} - \phi_s \right) - \frac{m L_{\text{emit}}}{\pi r_c^2 e^2} I_d^2 < \sigma_{en} v > \right]$$

$$+ \alpha \left[I_d \left(\frac{5}{2} T_{eV} - \phi_s \right) - \frac{m L_{\text{emit}}}{\pi r_c^2 e^2} C \ln \Lambda T_{eV}^{-3/2} I_d^2 + 2 \frac{m L_{\text{emit}}}{\pi r_c^2 e^2} I_d^2 < \sigma_{en} v > \right]$$

$$- \frac{m L_{\text{emit}}}{\pi r_c^2 e^2} I_d^2 < \sigma_{en} v > = 0, \quad (34)$$

where $C = 2.9 \times 10^{-12}$, and $\ln \Lambda \approx 10$ is the Coulomb logarithm. σ_{en} and σ_{ex} are the electron-neutral cross sections for elastic and excitation collisions, respectively. ϵ_{ex} is the average electron excitation energy. We use data from the Hayashi database[45] as retrieved from the LXCat website[46] for the electron-neutral, ionization, and excitation cross sections. The excitation cross section in Eqn. 34 is the *total* cross-section for all ground-state excitation reactions. The excitation energy is computed as the average of all excitation energies weighted by their respective Maxwellian-averaged reaction rates.

3. Orifice region

In the orifice, the energy equation can be considerably simplified by neglecting thermionic emission and electron backstreaming because of the higher sheath voltages due to the lower neutral densities than in the insert region. We obtain the following orifice energy balance

$$\alpha^2 \left[e n_g^2 < \sigma_{iz} v > \pi L_o r_o^2 \epsilon_i + e n_g^2 < \sigma_{ex} v > \pi L_o r_o^2 \epsilon_{ex} \right.$$

$$\left. + \frac{m L_o}{\pi r_o^2 e^2} C \ln \Lambda T_{eV}^{-3/2} I_d^2 - \frac{m L_o}{\pi r_o^2 e^2} I_d^2 < \sigma_{en} v > - \frac{5}{2} I_d \left(T_{eV} - T_{eV}^{\text{ins}} \right) \right]$$

$$+ \alpha \left[\frac{5}{2} I_d \left(T_{eV} - T_{eV}^{\text{ins}} \right) - \frac{m L_o}{\pi r_o^2 e^2} C \ln \Lambda T_{eV}^{-3/2} I_d^2 + 2 \frac{m L_o}{\pi r_o^2 e^2} I_d^2 < \sigma_{en} v > \right] - \frac{m L_o}{\pi r_o^2 e^2} I_d^2 < \sigma_{en} v > = 0, \quad (35)$$

where L_o is the orifice length and T_{eV}^{ins} is the insert electron temperature.

To obtain a relationship between the ionization fraction and neutral density, we use the conservation of mass applied to the sonic condition at the orifice outlet. It results in a quadratic equation for the ionization fraction.

$$\dot{m} = \pi r_o^2 \frac{1}{1 - \alpha} n_g M \sqrt{\gamma R_g \left(T_g + \alpha T_e \right)}, \quad (36)$$

Solving this equation and keeping the root for which $\alpha_o < 1$ gives an expression for the ionization fraction,

$$\alpha = 1 + \frac{1}{2 \bar{v}} \left(1 - \sqrt{4 \bar{v} \left(1 + \bar{T} \right) + 1} \right), \quad (37)$$

where $\bar{T} = T_g / T_e$ and $\bar{v}$ is given by

$$\bar{v} = \frac{1}{\gamma R_g T_e} \left(\frac{\dot{m}}{\pi r_o^2 n_g M} \right)^2 \quad (38)$$

The orifice energy equation (Eqn. 35) and the solution for the ionization fraction from conservation of mass (Eqn. 37) are combined to obtain a single equation for the unknown neutral density in the orifice.

D. Algorithm

Both the gas temperature and sheath voltage are free parameters. The expression for the sheath-edge density factor (Eqn. 29) is used in the pressure balance (Eqn. 19) to form an expression that depends only on α and n_g:

$$P = P_{mag} + P_{gd} + \left(\frac{r_c^2}{r_o^2} - 1\right) f_s \frac{\alpha_i}{1 - \alpha_i} n_g e T_{eV} \left(1 + \left(\frac{\alpha_i}{1 - \alpha_i}\right) f_s\right) + P_V^*. \tag{39}$$

To solve this equation, we use the perfect gas law to compute the total static pressure:

$$P = k_B n_g T_g + \frac{\alpha_i}{1 - \alpha_i} n_g e T_{eV} + \frac{\alpha_i}{1 - \alpha_i} n_g k_B T_g \tag{40}$$

Because we have used surface-integrated quantities when deriving the pressure balance, but re-expressed these terms using volume-averaged quantities, there are (at least) two possible choices for the definition of the total static pressure. Assuming constant total pressure in the insert region, we can either use the sheath-edge density or the volumetric value to compute this pressure. We choose the latter option because the sheath-edge terms balance the upstream portion, leaving only the pressure contribution on the orifice inlet.

Solving the system of equations resulting from the combination of the pressure balance (Eqn. 39), the perfect gas law (Eqn. 40), and the insert power balance (Eqn. 34) yields the solution for both n_g and α_i. We combine the expressions into a single equation for the unknown neutral density which we then solve using the bisection method in order to avoid solving the original multivariate nonlinear system. For each proposed insert neutral density and sheath potential, we solve for the ionization fraction in the insert using the insert power balance (Eqn. 34). The insert electron temperature is then obtained using the correlation in Eqn. 24. The orifice neutral density is calculated using the orifice power balance (Eqn. 35), mass continuity (Eqn. 37), and the insert electron temperature. The electron temperature for the orifice is then obtained using Eqn. 24, and the ionization fraction for the orifice is computed with Eqn. 37. Finally, the total pressure results calculated using the momentum balance (Eqn. 39) and the perfect gas law (Eqn. 40) are compared. If both results agree, the algorithm has converged and the solution is reported.

For a given geometry and gas, the orifice quantities depend on the mass flow rate, the discharge current, and the insert neutral density through the insert electron temperature. The orifice quantities can therefore be pre-computed and stored as a lookup table for faster computation. The upper bound for the orifice neutral density can obtained by imposing the conditions that $\alpha_o > 0$ and that the neutral density in the insert is greater than that in the orifice.

E. Wall temperature

We note that while the emission current has been eliminated from the model equations, the wall temperature may be retrieved from the total emitted current and the conservation of charge (Eqn. 27). The elimination of the emitted current from the model equations also removes the dependence of the pressure on the choice of emitter material, excluding any indirect dependence due to the heavy species temperature. Without the Schottky effect, the total emitted current is given by Richardson-Dushman's law,

$$I_{em} = 2\pi L_{\text{emit}} r_c D_{RD} T_c^2 \exp\left(-\frac{e\phi_w}{k_B T_c}\right), \tag{41}$$

where D_{RD} is the Richardson-Dushman constant, T_c is the emitter temperature, and ϕ_w is the work function. Because we have assumed that the emission length is defined such that the thermionic emission is thermally limited inside the active zone, the current extracted is not modified by space-charge limitation.

F. Sheath potential

The algorithm may also be used as an indirect method to compute the sheath potential. The total pressure calculated using the pressure balance (Eqn. 39) can be evaluated for multiple sheath potentials, and the intersections of the resulting family of pressure curves with the experimental pressure data can be used to estimate the variation of the sheath voltage over the experimental parameter range.

American Institute of Aeronautics and Astronautics

IV.   Results and discussion

We first show in this section the experimental results for the pressure measurement of the Princeton Large Hollow Cathode and then compare the results of the algorithm to experimental results. Additional experimental data are gathered from literature with data from the NSTAR,[38, 47, 48] the NEXIS,[49, 50] Friedly's cathode,[17] Salhi's cathode,[21] and the Jet Propulsion Laboratory's (JPL) 1.5 cm diameter LaB$_6$ cathode.[40] The dimensions and operating conditions of each cathode are shown in the Appendix (Table 1). They span a variety of geometries, gases, and operating conditions.

A.   Pressure measurements

Figure 5 shows pressure measurements we performed with and without the cathode discharge. Without a plasma, the pressure increases linearly with mass flow rate as is expected from a choked orifice. During operation the pressure increases both with mass flow rate and discharge current, a behavior similar to other cathodes.[17, 49, 51]
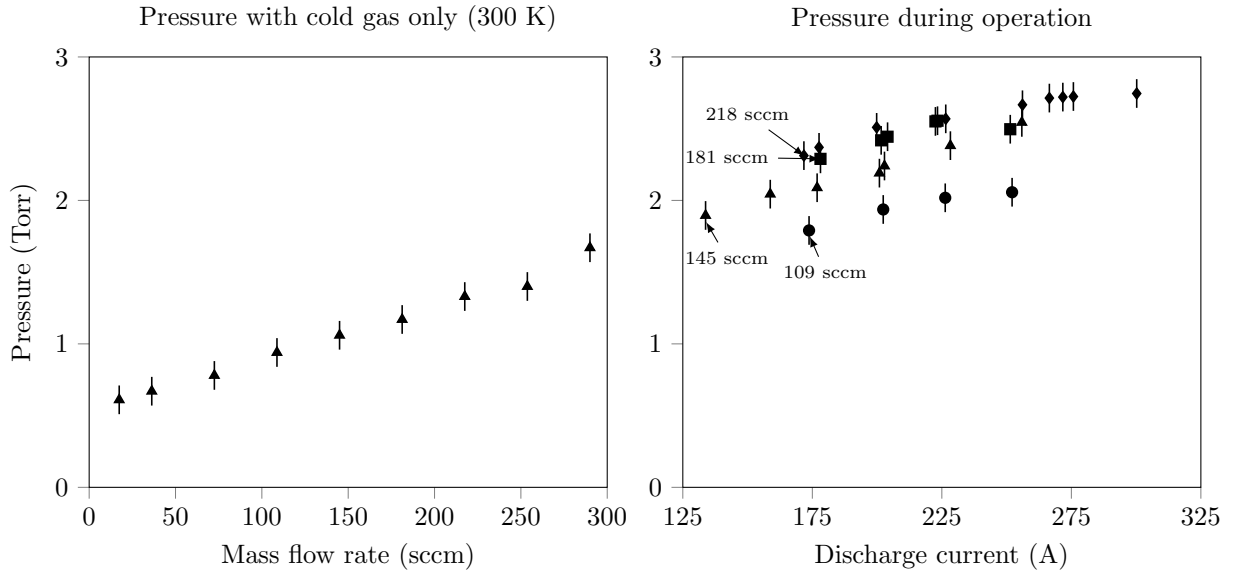

Figure 5: Total pressure measurements

B.   Algorithm verification

1.   Wall temperature

We show in Fig. 6 a comparison of our model to experimental data of the insert temperature. We applied the algorithm to both Salhi's cathode operating with argon and to the NSTAR cathode. The cathode wall temperature is reported in Refs. 21 and 48, respectively. We used the work function from Ref. 22 for the barium-oxide insert installed in the NSTAR cathode. Salhi's cathode uses a material with an estimated work function of 1.8–2.0 eV.[21] The results from our algorithm are averaged over all of the values tested for the two free parameters. We have performed sweeps with sheath voltages between 1 and 10 V and gas temperatures between 2000 K and 4000 K. The algorithm returns values within 10% of the experimental values for both cathodes. We find that the trend of the predicted wall temperature agrees with the experimental data, both with increasing discharge current and mass flow rate.

We also applied the algorithm to Friedly's cathode[17] with an estimated work function of 2 eV for the insert material (as reported in Ref. 13, p.91). We found results to be within 20% of experimental data, but did not have the same agreement as that of the NSTAR. We note that the temperatures reported by Friedly are that of the exterior of the cathode and are higher than the typical application range of barium-based emitters. We hypothesize that the emitter depleted its coating, especially at higher discharge currents, which would explain the reported high temperatures. The uncertainty in the work function of the material would explain
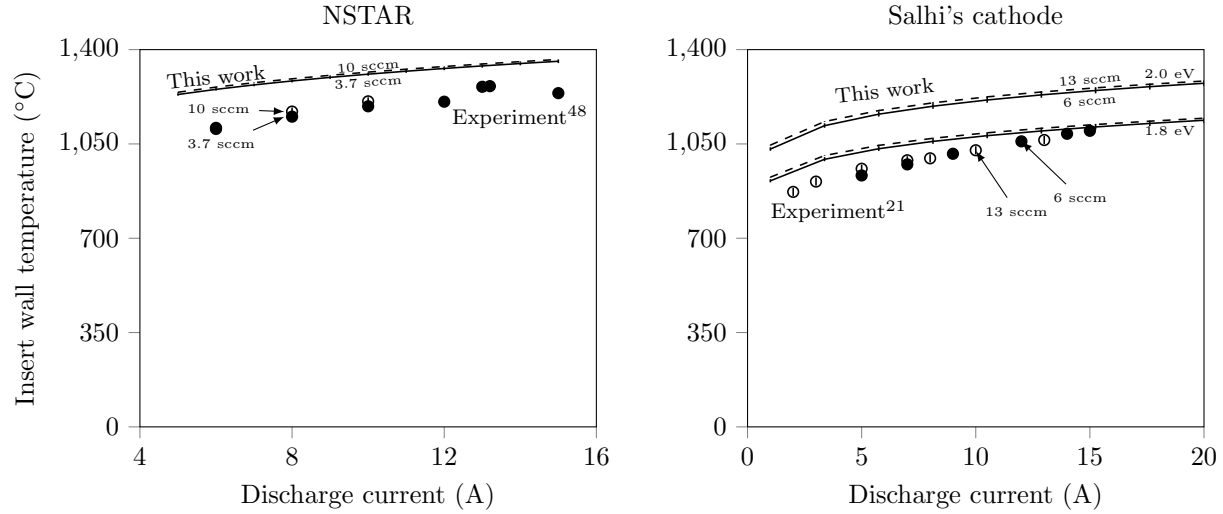
American Institute of Aeronautics and Astronautics

Figure 6: Left: Peak insert temperature of the NSTAR cathode. Right: cathode external wall temperature of Salhi's cathode. Error bars on the model indicate the minimum and maximum values obtained from a sweep of the two free parameters (sheath voltage and gas temperature) with values between 1–10 V and 2000–4000 K, respectively.

the discrepancy observed between the results of the model and the experimental measurements. We found that the observed trend of the results of the algorithm agrees with experimental results if we assume that the work function is that of tantalum (4.1 eV). Additionally, the assumptions made in Ref. 11 to estimate the emission length become invalid at high discharge currents for this particular cathode. The ionization fraction is indeed large in both the orifice (up to 60%) and in the insert (up to 30%) at high discharge currents and therefore challenges the assumption of charge-exchange-dominated ambipolar diffusion. A possible remedy is to include *all* interactions between particles when considering ambipolar diffusion.

2.   Electron temperature

Both predicted and experimental insert electron temperature are shown in Fig. 7 for the JPL's 1.5 cm LaB$_6$ hollow cathode[40] and for Salhi's cathode[21] operating on argon and with an orifice size of 1.21 mm. The insert electron temperature for the JPL's cathode is reported at the location of peak insert electron density. We use the highest reported values for Salhi's cathode, close to the peak insert electron density. We observe in all cases that the trend of decreasing electron temperature with increasing discharge current and mass flow rate is correctly captured. We note, however, that the electron temperature is over-predicted, which is a consequence of an under-prediction of the neutral density and is consistent with an under-predicted neutral gas pressure.

3.   Pressure prediction

We now compare the typical models used for calculating the pressure inside hollow cathodes to our algorithm for the NEXIS cathode. The models are delineated in Ref. 18. For the NSTAR cathode we also perform a comparison with results of a 2-D axisymmetric solver from Ref. 47. For the NEXIS, we compute the pressure for a gas temperature of 2,000 K for all models, and sheath voltages between 1 and 4 V. The results for the NSTAR are computed with 3,000 K and sheath voltages between 1 and 10 V. Results are shown in Fig. 8. Pressures predicted with both our theoretical model and the empirical correlation derived from literature data vary with discharge current and mass flow rate, while other existing models do not. These two approaches yield results that are close the experimentally measured pressure. Results for the NSTAR are similar to that of the 2-D axisymmetric solver, although the latter uses a discharge current 10% higher than the nominal current of 12 A. For cathodes that reasonably satisfy the model assumptions, the numerical algorithm allows us to bound the pressure for a cathode for which no pressure data are available.
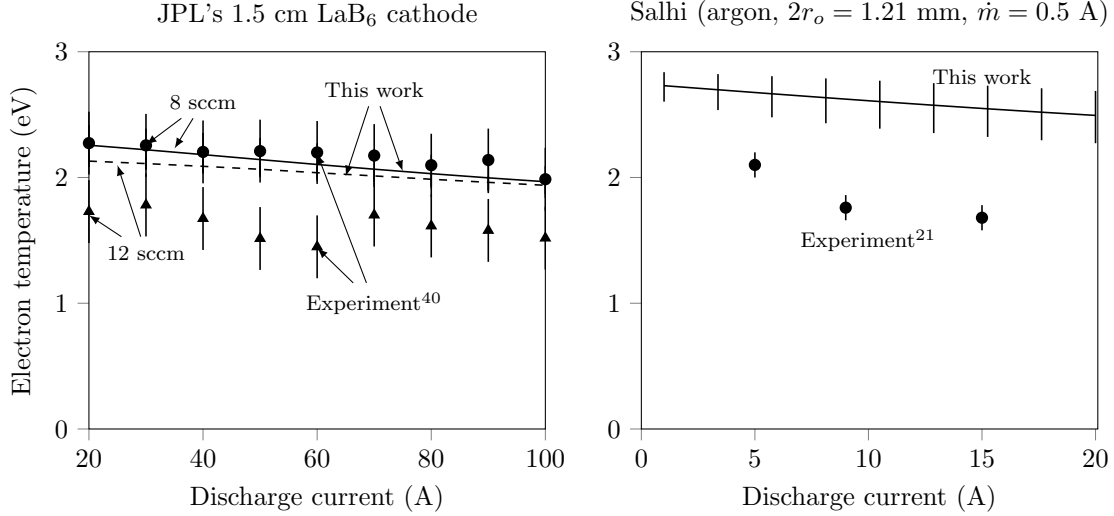
Figure 7: Comparison of calculated and experimentally measured insert electron temperature.

We note that in all cases, knowledge of the sheath potential is required. The family of curves generated by the model intersect experimental data at different sheath voltages. As mentioned in the previous section, this may be used to compute the sheath voltage from the experimental data.

C. Pressure scaling

1. Experimental data

Figure 9 shows the variation of the ratio of the measured pressure (P) to the magnetic pressure (P_{mag}). Results are presented as a function of the dimensionless ratio $I_d/\dot{m}$ where the mass flow rate is expressed in equivalent-Ampères. Experimental data suggest that $P/P_{mag} \propto (I_d/\dot{m})^{-r}$ where $1 < r < 2$. This trend is captured for most cathodes. The algorithm however overestimates the pressure for our cathode. We hypothesize that

- the magnetic pressure is overestimated because we did not take into account the net current of charged particles from the insert volume directed towards the orifice plate,

- gas leaks occur through the grafoil seals at graphite/stainless steel interfaces at high temperatures, thus decreasing the experimentally measured pressure, and

- gas leaks occur through the NPT fittings on the feed lines and pressure tap because they are sealed only with anti-seize compound as typical thread sealant compounds would not tolerate the operating temperature of the PLHC.

2. Theoretical approach

We obtain a scaling relationship for the total pressure by first rewriting the momentum balance (Eqn. 39) as

$$P = \left(\frac{\mu_0 I_d^2}{\pi r_o^2}\right)\left[\frac{1}{4\pi}\left(\frac{1}{4} + \ln\frac{r_c}{r_o}\right) + \left(\frac{\dot{m}_A}{I_d}\right)^2 \left(\frac{Mr_o}{\mu_0 e^2}\right)\left(\frac{1}{\pi r_o^3 n_g^o}\right)\left[1 + \frac{F(\gamma)}{\sqrt{1 + \alpha_o T_e/T_g}}\right] + \frac{P_{mf}}{\mu_0 I_d^2/\pi r_o^2}\right], \quad (42)$$

where the mass flow rate is in equivalent-Ampères, n_g^o is the orifice neutral density, and $F(\gamma)$ is a function of γ only:

$$F(\gamma) = \sqrt{2\pi}\gamma^{-1/2}\left(\frac{\gamma+1}{2}\right)^{1/\gamma+1}. \quad (43)$$

NSTAR
$\dot{m} = 3.7$ sccm

This work

Experiment[48, 49]

Empirical[18]

Domonkos[25]

Poiseuille

Pressure (Torr)

Discharge current (A)

NSTAR
$I_d = 12$ A

Experiment[48, 49]

Empirical[18]

This work

Mikellides[47]

Poiseuille

Domonkos[25]

Pressure (Torr)

Mass flow rate (sccm of Xe)

NEXIS
$\dot{m} = 5.5$ sccm

Poiseuille

Domonkos[25]

This work

Empirical[18]

Experiment[48, 49]

Pressure (Torr)

Discharge current (A)

NEXIS
$I_d = 22$ A

Poiseuille

Domonkos[25]

Empirical[18]

This work

Experiment[48, 49]

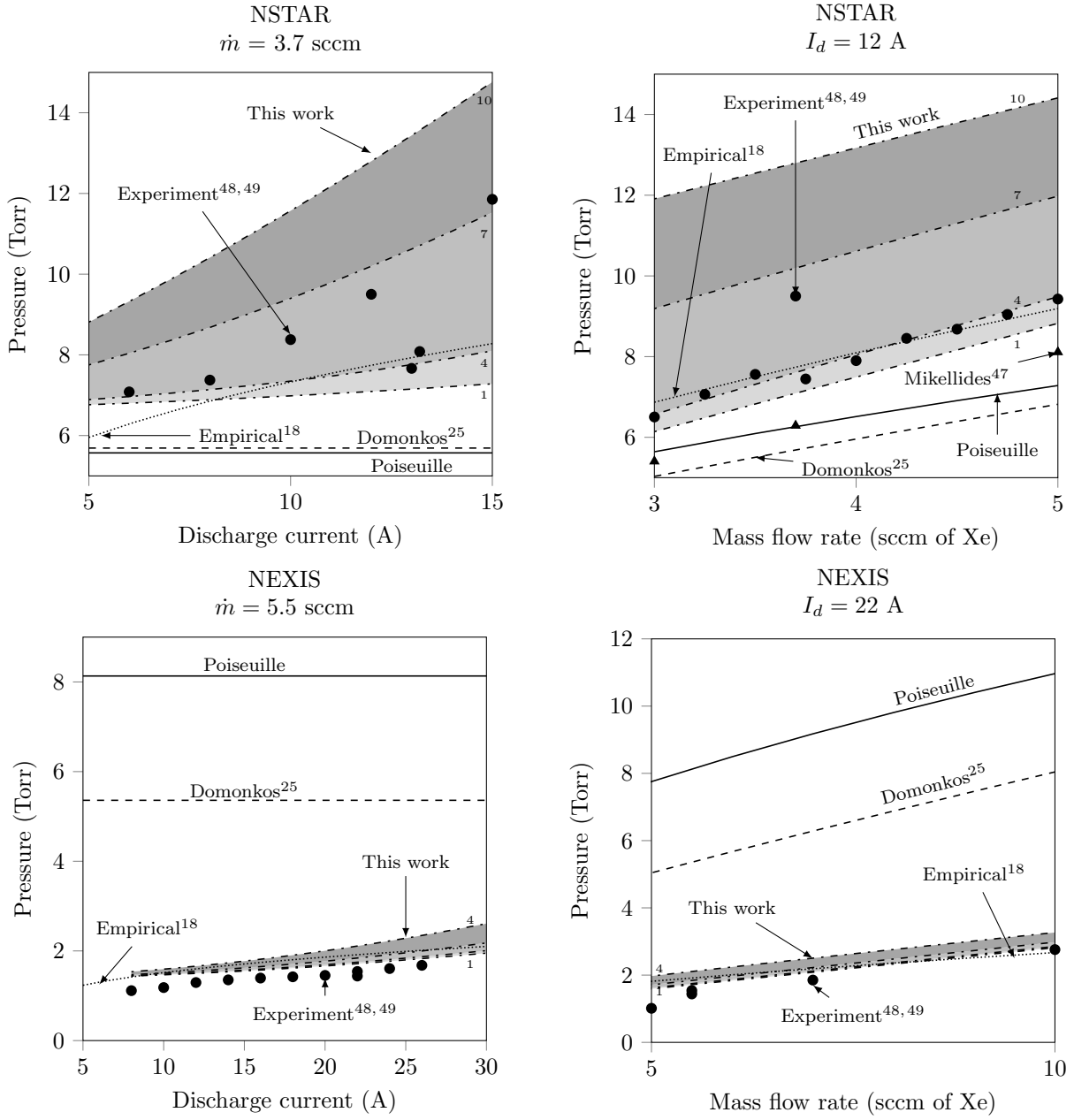Pressure (Torr)

Mass flow rate (sccm of Xe)

Figure 8: Comparison of pressure models used for the calculation of the total pressure inside hollow cathodes.

We show in Fig. 10 the variation with discharge current of the ionization fraction, the quantity $< \sigma_{iz} v > T_{eV}^{1/2}$ which appears in the sheath-edge ratio, the orifice neutral density, and the term $\sqrt{1 + \alpha_o T_e/T_g}$ that appears in the above equation. The results are shown for a single illustrative cathode (NSTAR cathode with mass flow rate of 3.7 sccm) for the given quantity averaged over the entire parameter space (neutral temperature varying from 2,000 K to 4,000 K and sheath voltages between 1 and 10 V). Similar results are obtained with other cathodes. For a *given mass flow rate*, we can approximate the variation of those quantities with a semi-empirical functional form:

$$\sqrt{1 + \alpha_o T_e/T_g} = C_{s,0} + C_{s,1} I_d + C_{s,2} I_d^2, \tag{44}$$

$$\alpha_i = C_\alpha I_d^\eta, \text{ and} \tag{45}$$

$$n_g^o = C_{n,0} + C_{n,1} I_d. \tag{46}$$

In the region of typical operation of hollow cathodes (pressure-diameter product greater than 1), the term that appears in the sheath-edge ratio can be given as $< \sigma_{iz} v > T_{eV}^{1/2} = C_\sigma \left(Pd\right)^2$.

From Eqn. 42 we can now write the ratio of total to magnetic pressure as

$$\frac{P}{P_{mag}} = 1 + k_1 \left(\frac{\dot{m}_A}{I_d}\right)^2 \frac{1}{1 + C_{n,1}/C_{n,0} I_d} \left(1 + \frac{F(\gamma)}{C_{s,2} I_d^2 + C_{s,1} I_d + C_{s,0}}\right) + k_2 I_d^{\eta-2}, \tag{47}$$

where the two constants k depend on gas, geometry, and chosen value of heavy particle temperature:

$$k_1 = \left(\frac{M r_o}{\mu_0 e^2}\right) \left(\frac{1}{\pi r_o^3 C_{n,0}}\right) \frac{1}{\frac{1}{4\pi}\left(\frac{1}{4} + \ln \frac{r_c}{r_o}\right)}, \text{ and} \tag{48}$$

$$k_2 = \frac{\pi r_o^2 e}{8\mu_0 r_c} \sqrt{\frac{M}{e}} C_\alpha C_\sigma \left(\frac{r_c^2}{r_o^2} - 1\right) \frac{1}{(k_B T_g)^2} \frac{1}{\frac{1}{4\pi}\left(\frac{1}{4} + \ln \frac{r_c}{r_o}\right)}. \tag{49}$$

To obtain k_2 in this form we assumed that $\alpha_i \ll 1$ and $f_s \ll 1$. We also assumed that the flow was purely molecular ($\theta = 1$) at the orifice outlet to obtain k_1. The rational function in the discharge current that arises from the orifice neutral density can always be approximated by a power law in a region where the two functions $1/(1 + x)$ and b/x^δ are reasonably close. This region can be defined as the values of x, b, and δ such that the Taylor expansion of either function around any point x_0 are equal to the first order or differ only by numerical constant $\epsilon \ll 1$. This in turn means that the gasdynamic term can be rewritten as

$$\left(\frac{\dot{m}_A}{I_d}\right)^2 \frac{1}{1 + C_{n,1}/C_{n,0} I_d} \propto \left(\frac{\dot{m}_A}{I_d}\right)^{2-\delta} \dot{m}_A^\delta. \tag{50}$$

We recognize in $2 - \delta$ the exponent r suggested by the experimental data.

We note that the dimensional total pressure can be written as

$$P = a I_d^2 + b \frac{\dot{m}_A^2}{1 + c I_d} \left(1 + G\left(I_d\right)\right) + d I_d^\eta, \tag{51}$$

where a, b, c, d, and G are found from the above expressions. We recognize in the total pressure scaling (Eqn. 51) the magnetic pressure ($\propto I_d^2$), the gasdynamic pressure ($\propto \dot{m}^2$) modified to take into account the plasma effects ($\propto 1/\left(1 + c I_d\right)\left(1 + G\left(I_d\right)\right)$) and an additional momentum flux term from the ions that are accelerated towards the orifice plate ($\propto I_d^\eta$). At low current ($I_d \to 0$) the polynomials with the discharge current terms become constant, the momentum flux term vanishes, and we recover the conservation of momentum for a gas flowing through an orifice plate. At high current ($I_d \to +\infty$) the expression becomes

$$P = a I_d^2 + b^* \frac{\dot{m}_A^2}{I_d} + f I_d^\eta, \tag{52}$$

which indicates that magnetic pressure and momentum flux terms become dominant. In the intermediate range, however, all terms must be kept.

V.   Conclusion

Based on the lessons learned in our review of prior cathode modeling efforts,[10] we have developed a 0-D model for orificed hollow cathodes and computed volume-averaged plasma quantities for a large variety of cathodes and operating conditions. Good agreement is obtained with both literature data and with experimental pressure data we gathered on our own large hollow cathode running on argon at up to 300 A of discharge current. We have uncovered a scaling relationship for the total pressure with both mass flow rate and discharge current and have given a physical interpretation for it.

We were able to bound both the sheath potential and neutral gas temperature and found that the solutions of the algorithm are not sensitive to these parameters. These two parameters can be self-consistently incorporated into the model through a potential solver and the energy equation for the heavy particles, respectively. The values for the neutral gas temperature remain to be experimentally validated.

This work can be used in conjunction with the charge-exchange-dominated ambipolar diffusion model for the insert region we presented in Ref. 11 to find the electron density distribution within a hollow cathode. We also note that the proposed model is not limited to the study of scaling relationships for the total pressure. The model can also be applied to the study of additional scaling relationships, for example the variation of electron temperature or attachment length as a function of discharge current and mass flow rate, which would illuminate the underlying physics of thermionic orificed hollow cathodes. The model is also a building block for insert performance prediction if coupled to an erosion model for the thermionic material and for cathode performance prediction if coupled to a cathode thermal and plume model.
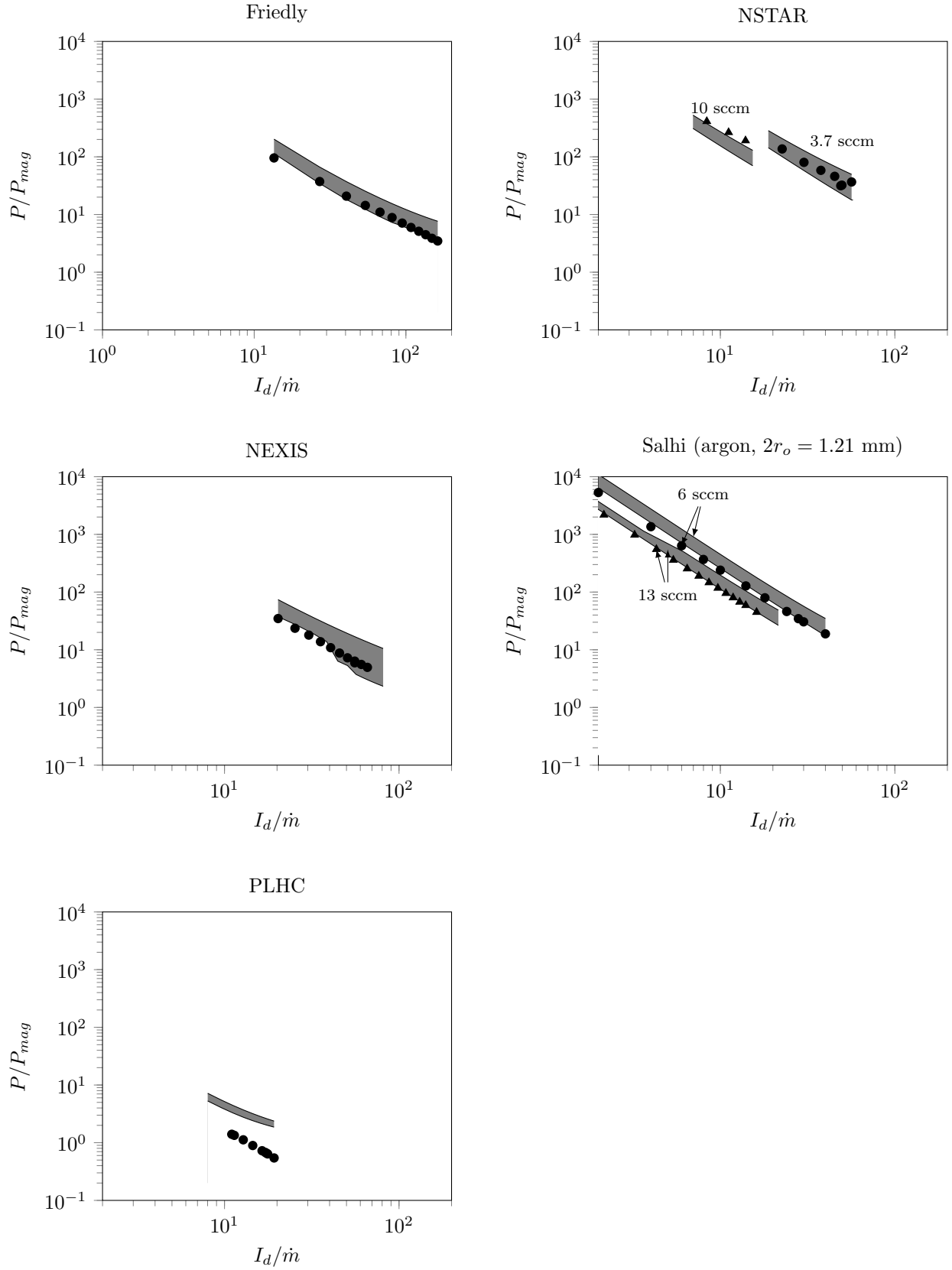
Acknowledgments

Figure 9: Variation of the total-to-magnetic-pressures ratio (P/P_{mag}) as function of discharge current to mass flow rate ratio $(I_d/\dot{m})$. The shaded area bounds the results of the sweeps on all of the free parameters.

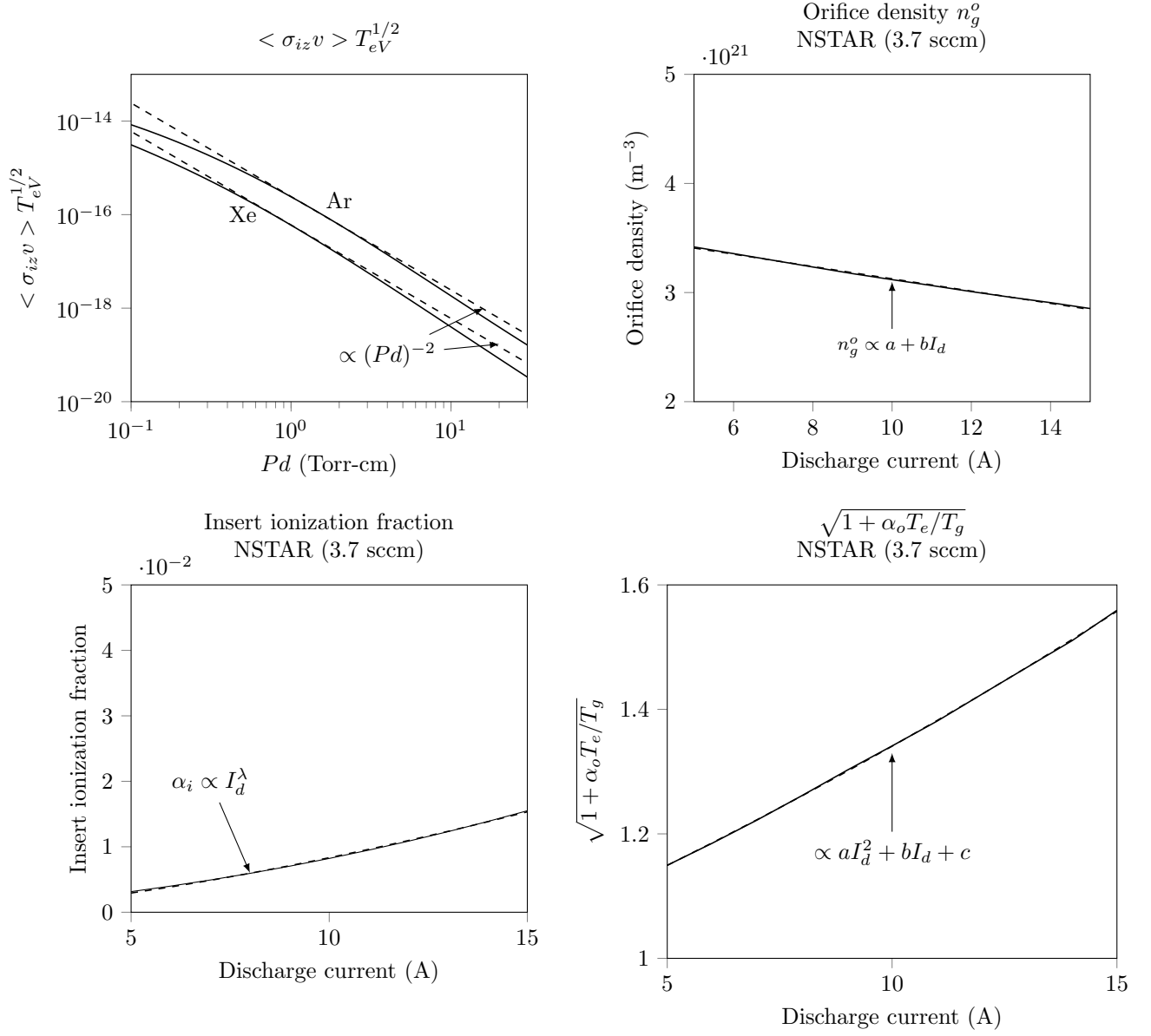American Institute of Aeronautics and Astronautics

Figure 10: Variation of quantities necessary to find a scaling relationship for the total pressure. While results are shown for the NSTAR only, other cathodes follow similar trends.

References

[1] Brown, D. L., Beal, B. E., and Haas, J. M., "Air Force Research Laboratory High Power Electric Propulsion Technology Development," *IEEE Aerospace Conference*, 2010.

[2] Goebel, D. M. and Chu, E., "High Current Lanthanum Hexaboride Hollow Cathodes for High Power Hall Thrusters," *32nd International Electric Propulsion Conference*, 2011, IEPC-2011-053.

[3] Hofer, R., Randolph, T., Oh, D., Snyder, J., and de Grys, K., "Evaluation of a 4.5 kW Commercial Hall Thruster System for NASA Science Missions," *42nd AIAA/ASME/SAE/ASEE Joint Propulsion Conference & Exhibit*, 2006, AIAA-2006-4469.

[4] Plasek, M., Wordingham, C. J., Rojas Mata, S., Luzarraga, N., and Choueiri, E. Y., "Experimental Investigation of a Large Diameter Cathode," *50th AIAA/ASME/SAE/ASEE Joint Propulsion Conference & Exhibit*, 2014, AIAA-2014-3825.

[5] Goebel, D. M. and Chu, E., "High-Current Lanthanum Hexaboride Hollow Cathode for High-Power Hall Thrusters," *Journal of Propulsion and Power*, Vol. 30, No. 1, 2014, pp. 35–40.

[6] Hall, S. J., Jorns, B. J., Gallimore, A. D., Kamhawi, H., Haag, T. W., Mackey, J. A., Gilland, J. H., Peterson, P. Y., and Baird, M., "High-power performance of a 100-kW class nested Hall thruster," *35th International Electric Propulsion Conference*, 2017, IEPC-2017-228.

[7] Jorns, B., Gallimore, A. D., Hall, S. J., Peterson, P. Y., Gilland, J. E., Goebel, D. M., Hofer, R., and Mikellides, I., "Update on the Nested Hall Thruster Subsystem for the NextSTEP XR-100 Program," *AIAA Propulsion and Energy Forum*, 2018.

[8] Wordingham, C. J., Taunay, P.-Y. C. R., and Choueiri, E. Y., "Multiple-Kilowatt-Class Graphite Heater for Large Hollow Cathode Ignition," *51st AIAA/SAE/ASEE Joint Propulsion Conference & Exhibit*, 2015, AIAA-2015-4010.

[9] Goebel, D. M., Becatti, G., Reilly, S., Tilley, K., and Hall, S. J., "High Current Lanthanum Hexaboride Hollow Cathode for 20-200 kW Hall Thrusters," *35th International Electric Propulsion Conference*, 2017, IEPC-2017-303.

[10] Wordingham, C. J., Taunay, P.-Y. C. R., and Choueiri, E. Y., "A Critical Review of Orificed Hollow Cathode Modeling: 0-D Models," *53rd AIAA/SAE/ASEE Joint Propulsion Conference & Exhibit*, 2017, AIAA-2017-4888.

[11] Wordingham, C. J., Taunay, P.-Y. C. R., and Choueiri, E. Y., "Theoretical Prediction of the Dense-Plasma Attachment Length in an Orificed Hollow Cathode," *35th International Electric Propulsion Conference*, 2017, IEPC-2017-566.

[12] Siegfried, D. E. and Wilbur, P. J., "Studies on an experimental quartz tube hollow cathode," *14th International Electric Propulsion Conference*, 1979.

[13] Siegfried, D. E., *A Phenomenological Model for Orificed Hollow Cathodes*, Ph.d., Colorado State University, 1982.

[14] Siegfried, D. E. and Wilbur, P. J., "Phenomenological Model Describing Orificed, Hollow Cathode Operation," *AIAA Journal*, Vol. 21, No. 1, 1983, pp. 5–6.

[15] Siegfried, D. E. and Wilbur, P. J., "A model for mercury orificed hollow cathodes - Theory and experiment," *AIAA journal*, Vol. 22, No. 10, 1984, pp. 1405–1412.

[16] Wilbur, P. J., "Advanced Ion Thruster Research," Tech. Rep. CR-168340, NASA, 1984.

[17] Friedly, V. J., "Hollow Cathode Operation at High Discharge Currents," 1990, M.Sc.

[18] Taunay, P.-Y. C. R., Wordingham, C. J., and Choueiri, E. Y., "An Empirical Scaling Relationship for the Total Pressure in Hollow Cathodes," *AIAA Propulsion and Energy Forum*, 2018, AIAA-2018-4428.

[19] Siegfried, D. E. and Wilbur, P. J., "An investigation of mercury hollow cathode phenomena," *13th International Electric Propulsion Conference*, 1978.

[20] Salhi, A. and Turchi, P. J., "Theoretical Modeling of Orificed Hollow Cathode Discharges," *23rd International Electric Propulsion Conference*, 1993, IEPC-1993-024.

[21] Salhi, A., *Theoretical and experimental studies of orificed, hollow cathode operation*, Ph.d., The Ohio State University, 1993.

[22] Goebel, D. and Katz, I., *Fundamentals of Electric Propulsion: Ion and Hall Thrusters*, John Wiley & Sons, Inc., 2008.

[23] Mizrahi, J. P., Vekselman, V., Krasik, Y., and Gurovich, V., "0-D Plasma Model for Orificed Hollow Cathodes," *32nd International Electric Propulsion Conference*, 2011, IEPC-2011-334.

[24] Mizrahi, J., Vekselman, V., Gurovich, V., and Krasik, Y. E., "Simulation of Plasma Parameters During Hollow Cathodes Operation," *Journal of Propulsion and Power*, Vol. 28, No. 5, 2012, pp. 1134–1137.

[25] Domonkos, M. T., *Evaluation of low-current orificed hollow cathodes*, Ph.d., University of Michigan, 1999.

[26] Domonkos, M. T., "A Particle and Energy Balance Model of the Orificed Hollow Cathode," *38th AIAA/ASME/SAE/ASEE Joint Propulsion Conference & Exhibit*, 2002, AIAA-2002-4240.

[27] Albertoni, R., *Cathode Processes in MPD Thrusters*, Ph. d., Universita Degli Studi di Pisa, 2012.

[28] Albertoni, R., Pedrini, D., Paganucci, F., and Andrenucci, M., "A Reduced-Order Model for Thermionic Hollow Cathodes," *IEEE Transactions on Plasma Science*, Vol. 41, No. 7, 2013, pp. 1731–1745.

[29] Wordingham, C. J., Taunay, P.-Y. C. R., and Choueiri, E. Y., "Multi-kilowatt Class Heaters for Large Hollow Cathodes," *Review of Scientific Instruments*, Vol. 87, No. 7, 2018.

[30] Mandell, M. J. and Katz, I., "Theory of Hollow Cathode Operation in Spot and Plume Modes," *30th AIAA/ASME/SAE/ASEE Joint Propulsion Conference & Exhibit*, 1994, AIAA-1994-3134.

[31] Katz, I., Gardner, B., Jongeward, G., Patterson, M., and Myers, R., "A model of plasma contactor behavior in the laboratory," *34th Aerospace Sciences Meeting and Exhibit*, 1996, AIAA-1996-0484.

[32] Katz, I., Gardner, B. M., Mandell, M. J., Jongeward, G. A., Patterson, M., and Myers, R. M., "Model of Plasma Contactor Performance," *Journal of Spacecraft and Rockets*, Vol. 34, No. 6, 1997.

[33] Katz, I., Mandell, M. J., Patterson, M., and Domonkos, M., "Sensitivity of Hollow Cathode Performance to Design and Operating Parameters," *35th AIAA/ASME/SAE/ASEE Joint Propulsion Conference & Exhibit*, 1999, AIAA-1999-2576.

[34] Katz, I., Anderson, J., Polk, J., and Brophy, J., "A Model of Hollow Cathode Plasma Chemistry," *38th AIAA/ASME/SAE/ASEE Joint Propulsion Conference & Exhibit*, 2002, AIAA-2002-4241.

[35]Katz, I., Anderson, J. R., Polk, J. E., and Brophy, J. R., "One-Dimensional Hollow Cathode Model," *Journal of Propulsion and Power*, Vol. 19, No. 4, 2003, pp. 595–600.

[36]Jobson, D. A., "On the flow of a compressible fluid through orifices," *Proceedings of the Institution of Mechanical Engineers*, Vol. 169, No. 1, 1955, pp. 767–776.

[37]Prewett, P. and Allen, J., "The double sheath associated with a hot cathode," *Proceedings of the Royal Society of London A: Mathematical, Physical and Engineering Sciences*, Vol. 348, The Royal Society of London, 1976, pp. 435–446.

[38]Jameson, K. K., Goebel, D. M., and Watkins, R. M., "Hollow Cathode and Keeper-Region Plasma Measurements," *41st AIAA/ASME/SAE/ASEE Joint Propulsion Conference & Exhibit*, 2005, AIAA-2005-3667.

[39]Goebel, D. M., Jameson, K. K., Watkins, R. M., Katz, I., and Mikellides, I. G., "Hollow cathode theory and experiment. I. Plasma characterization using fast miniature scanning probes," *Journal of Applied Physics*, Vol. 98, No. 11, 2005.

[40]Chu, E. and Goebel, D. M., "High-current lanthanum hexaboride hollow cathode for 10-to-50-kW hall thrusters," *IEEE Transactions on Plasma Science*, Vol. 40, No. 9, 2012, pp. 2133–2144.

[41]Jahn, R. G., *Physics of Electric Propulsion*, Dover Publications, 2006, p.244.

[42]Santeler, D. J., "Exit loss in viscous tube flow," *Journal of Vacuum Science & Technology A: Vacuum, Surfaces, and Films*, Vol. 4, No. 3, 1986, pp. 348–352.

[43]Livesey, R. G., *Foundations of Vacuum Science and Technology*, chap. Flow of Gases Through Tubes and Orifices, John Wiley & Sons, Inc, 1998, pp. 135–137.

[44]Cassady, L., *Lithium-fed Arc Multichannel and Single-Channel Hollow Cathode: Experiment and Theory*, Ph.D. thesis, Princeton University, 2006, pp.105–110.

[45]Hayashi, M., "Bibliography of Electron and Photon Cross Sections with Atoms and Molecules Published in the 20th Century - Xenon," Tech. Rep. NIFS-DATA-79, NIFS, 2003.

[46]"Hayashi database," `http://www.lxcat.net`, Retrieved on Jun. 28, 2019.

[47]Mikellides, I. G., "Effects of Viscosity in a Partially Ionized Channel Flow with Thermionic Emission," *Physics of Plasmas*, Vol. 16, 2009.

[48]Polk, J., Grubisic, A., Taheri, N., Goebel, D. M., and Hornbeck, S. E., "Emitter Temperature Distributions in the NSTAR Discharge Hollow Cathode," *41st AIAA/ASME/SAE/ASEE Joint Propulsion Conference & Exhibit*, 2005, AIAA-2005-4398.

[49]Jameson, K. K., Goebel, D. M., and Watkins, R. M., "Hollow Cathode and Thruster Discharge Chamber Plasma Measurements Using High-Speed Scanning Probes," *29th International Electric Propulsion Conference*, 2005, IEPC-2005-269.

[50]Goebel, D. M. Jameson, K. K. and Katz, I., "Hollow Cathode and Keeper-Region Plasma Measurements Using Ultra-Fast Miniature Scanning Probes," *40th AIAA/ASME/SAE/ASEE Joint Propulsion Conference & Exhibit*, 2004, AIAA-2004-3430.

[51]Patterson, S. W. and Fearn, D. G., "The Generation of High Energy Ions in Hollow Cathode Discharges," *26th International Electric Propulsion Conference*, 1999, pp. 695–702, IEPC-1999-125.

[52]Mikellides, I. G., Katz, I., Goebel, D. M., and Polk, J. E., "Hollow cathode theory and experiment. II. A two-dimensional theoretical model of the emitter region," *Journal of Applied Physics*, Vol. 98, 2005.

[53]Mikellides, I. G., Katz, I., Goebel, D. M., Polk, J. E., and Jameson, K. K., "Plasma processes inside dispenser hollow cathodes," *Physics of Plasmas*, Vol. 13, 2006.

Appendix

Cathodes studied

Cathode	Dimension				Gas	$\dot{m}$	I_d
	Insert		Orifice				
	L (cm)	I.D. (cm)	L (mm)	D (mm)		(sccm)	(A)
NSTAR Discharge[38, 47, 48]	2.54	0.38	0.74	1.02	Xe	$2.47 - 10.0$	$5.95 - 15$
NEXIS[49, 50]	2.54	1.27*	0.74†	$1.5 - 2.8$		4–10	4–32
Friedly[17]	2.5	0.47	1.0‡	0.74		$2.5 - 6.4$	5–60
JPL 1.5 cm LaB$_6$ cathode[40]	2.54	0.7	1.0‡	0.38		8–12	20–100
Salhi[21]	2.54	0.38	1.24	1.21	Ar	6, 13	2–20
Princeton	8.0	2.715	1.5	0.8		109–218	125–325

* Refs. 52,53 consider an insert inner diameter of 1.20 cm, though later work by Goebel and Katz[22] suggest an insert diameter of 1.27 cm.

† Measured from plots in Ref. 53.

‡ The length of the orifice is not specified an is set to 1 mm.

Table 1: Dimensions of the benchmark cathodes.

Correlation coefficients

Species	Quantity	Index		
		0	1	2
Xe	T_{eV}	1.3	0.34	0.48
	L_{emit}	0.75	1.0	3.0
Ar	T_{eV}	1.91	0.341	0.945
	L_{emit}	0.86	0.613	1.89

Table 2: The coefficients used for the insert electron temperature and attachment length correlations (Eqns. 24 and 26).

Species	Temperature	Index			
		0	1	2	3
Xe	2000 K	1.230	-0.0052	0.313	0.429
	3000 K	1.290	-0.0062	0.337	0.503
	4000 K	1.300	-0.0068	0.365	0.591
Ar	2000 K	1.889	-0.0197	0.287	0.793
	3000 K	1.941	-0.0250	0.320	0.935
	4000 K	1.723	-0.0257	0.401	1.250

Table 3: The coefficients used for the orifice electron temperature (Eqn. 24).